

9. W. H. Michael, R. H. Tolson, A. P. Mayo, W. T. Blackshear, M. B. Kelly, D. L. Cain, J. P. Brenkle, I. I. Shapiro, R. D. Reasenberg, *ibid.*, p. 803.
10. R. W. Shorthill, R. E. Hutton, H. J. Moore, II, R. F. Scott, C. R. Spitzer, *ibid.*, p. 805.
11. B. C. Clark, P. Toulmin, III, A. K. Baird, K. Keil, H. J. Rose, Jr., *ibid.*, p. 804.
12. The Viking mission is a part of NASA's Office of Space Science Planetary Exploration Program and is managed by the Langley Research Center. The orbiter was built by the Jet Propulsion Laboratory and its subcontractors; the lander by Martin Marietta Corporation and its subcontractors. The launch vehicle was provided by Lewis Research Center. The mission's operations are conducted by a 750-man Viking flight

team, managed by the Langley Research Center. The flight team is a totally integrated organization, staffed by personnel from NASA, JPL, Martin Marietta, their subcontractors, and all of the Viking scientists. The effort is the result of thousands of dedicated men and women who provided the ingenuity, the loyalty, the perseverance, and the faith in our future to make the Viking mission possible. A special note of thanks goes to the student interns for their technical assistance. The interns were supported by grants from the Alfred P. Sloan Foundation and NASA. Finally, it should be recognized that the project was organized and led by James S. Martin, A. T. Young, B. T. Lee, P. Lyman, and J. Goodlett.

26 July 1976

Preliminary Results from the Viking Orbiter Imaging Experiment

Abstract. During its first 30 orbits around Mars, the Viking orbiter took approximately 1000 photographic frames of the surface of Mars with resolutions that ranged from 100 meters to a little more than 1 kilometer. Most were of potential landing sites in Chryse Planitia and Cydonia and near Capri Chasma. Contiguous high-resolution coverage in these areas has led to an increased understanding of surface processes, particularly cratering, fluvial, and mass-wasting phenomena. Most of the surfaces examined appear relatively old, channel features abound, and a variety of features suggestive of permafrost have been identified. The ejecta patterns around large craters imply that fluid flow of ejecta occurred after ballistic deposition. Variable features in the photographed area appear to have changed little since observed 5 years ago from Mariner 9. A variety of atmospheric phenomena were observed, including diffuse morning hazes, both stationary and moving discrete white clouds, and wave clouds covering extensive areas.

This report is a preliminary assessment of pictures acquired from the Viking 1 orbiter during its first 30 orbits (designated as revs). During this period, attention was focused on the selection of landing sites. However, the pictures acquired have broad scientific interest, both for geology and for studies of the martian atmosphere.

The Viking visual imaging system (VIS) (1) consists of two high-resolution, slow-scan television framing cameras. Conceptually similar to the Mariner camera systems used in previous Mars, Mercury, and Venus missions, the VIS incorporates improvements designed to increase both spatial resolution and coverage. Each camera employs a 475-mm diffraction limited telescope and a 37-mm-diameter vidicon, the central region of which is scanned with a raster format of 1056 lines by 1182 samples and produces a 1.54° by 1.69° field of view. The optical axes of the cameras are offset by 1.38°. Cameras are shuttered alternately, resulting in contiguous swaths of images 80 km wide, with resolution better than 100 m near periapsis. Six color filters are available to restrict the image spectral bandpass to limited portions of the cameras' near-visual response characteristics.

The orbiter imaging experiment start-

ed acquiring calibration data 50 days before Mars orbit insertion (MOI); acquisition of scientific Mars data did not, however, begin until 120 hours before MOI when red and violet picture pairs were acquired every 4 hours. Beginning at MOI-56 hours, three-color pictures were taken every 2 hours through MOI-25 hours. A series of pictures taken with the red, the minus blue, and the violet filters completed the approach imaging. These early frames allayed any fears that the planet's atmosphere would interfere with photographing the surface. In several regions, particularly Hellas, Argyre, and Memnonia, they also revealed local brightenings interpreted as surface frost or ice clouds low in the atmosphere. One surprise was the visibility of the surface in the regions of the south pole, where a hood of clouds had been anticipated. After MOI, the orbiter cameras were devoted to finding suitable sites for the Viking landers.

Prior to insertion, detailed plans had been formulated to evaluate potential hazards at the landing site (A1) at 19°N, 34°W (Fig. 1), near the mouth of the large Chryse channels at the southern edge of the Chryse basin. The plan involved a calibration sequence on rev 1, extended coverage of the A1 site area on rev 3, and stereo coverage of the specific land-

ing area on revs 4, 6, and 8. Because of a delayed arrival at the planet, the rev 1 observations were not made; the first high-resolution frames were acquired on rev 3. These revealed surprising detail in the A1 area (discussed below), sufficient to cause apprehension about its suitability as a landing site. Consequently, it was decided to look elsewhere for a safer site. The region to the northwest of the original site appeared most likely to yield a smooth area because it is farther from the mouths of the large channels, close to the deepest part of the Chryse basin, and might therefore be a site of fluvial deposition. This area (A1NW) did appear smooth in the pictures. Radar data (2) acquired later, however, indicated adverse conditions and resulted in searches on revs 20 and 22 for additional sites to the west, where a suitable site was eventually found. During this period two sites for the second lander were also examined (Fig. 1). These are the B site at 10°W, 44°N (revs 9 and 26) and the C site at 44°W, 6°S (revs 12 and 14). While the low-altitude coverage was being acquired, high-altitude observations continued to monitor atmospheric activity.

The Chryse Planitia region. Regional and local geological analyses (3) on the basis of pre-Viking data show that the area consists of relatively smooth plains of Chryse Planitia near the terminus of three large channel systems (Ares Vallis, Tiu Vallis, and Simud Vallis) that originate in chaotic terrain of Margaritifer Sinus and drain northward into the Chryse basin (Fig. 1). These channels and their associated tributary networks are considered to be primarily fluvial in origin and to have been modified by aeolian processes; however, the degree of modification by wind has not been established.

The predominant feature in the A1 area is lightly cratered plains typified by ridges similar to those on the lunar maria, and which increase in frequency and prominence to the northwest. By analogy to lunar geology, presence of the ridges suggests that the plains are lava flows with low viscosity in the melting range and are probably of basaltic composition. The second most extensive unit in the area forms plateaus which stand topographically above the plains. These are probably remnants of a surface that is older than the lava plains. Almost everywhere in this region streamlined plateau forms indicate sculpturing by fluid flow. In the transition zone between the Chryse basin and the cratered uplands, individual impact craters formed effective barriers to flow; downstream

from the barriers the plateaus form islands with teardrop shapes (Fig. 2). Many plateau remnants are regularly terraced, possibly as a result of differential erosion of strata in the plateau material, or they could represent terraces from progressively lower fluvial levels. Toward the northwest the outliers of plateau material are less affected by the channeling process and appear to have undergone erosion by mass wasting along the margin, producing hummocky terrain.

In the southwest part of the A1 area, the lightly cratered plains have been etched, or stripped away in angular patches, to reveal a light toned, topographically lower, and presumably stratigraphically older unit (Fig. 3). Two possible agents of removal are wind and water. The exact stripping process is not known but the removal of material has been influenced by local structure. The general trend of the etched zone is parallel to Tiu Vallis and suggests a genetic relation to the formation of the channel. The northern end of the etched zone grades into incipient chaotic terrain, indicating that the etching may have been initiated or enhanced by ground-sapping processes.

At about 37.5°W and 22.5°N, 250 km northwest of the original A1 site, a channel segment possibly related to Tiu Vallis cuts through plateau material. The floor of the channel in this area is characterized by a network of fractures that are several hundred meters wide and several kilometers long. The general trend of the fracture system is parallel with the channel; a less pronounced set of fractures is transverse to the channel axis.

Knobs occur throughout the plains unit and range in size from several hundred meters to several kilometers across. They appear to be of diverse origin—some have distinct summit craters and are interpreted as volcanic in origin (perhaps cinder cones), others appear to be erosional remnants of plateau material, and still others are undoubtedly remnants of degraded and nearly buried crater rims. Small pancake-shaped features superimposed on both plains and etched terrain are interpreted to be constructional features possibly of volcanic origin (Fig. 3). Central craters and knobs, and possible dikes, support this interpretation.

On rev 10, 80 frames were taken of an area centered at 23°N, 43°W, close to the center of the Chryse basin (Fig. 1). It was anticipated that the region would be free of the fluvial features, etched terrain, and upland remnants that character-

ized the original A1 area. This prediction was largely fulfilled. Most of the area consists of lightly cratered plains, which in the western part are typified by north-south trending marelike ridges. Two islandlike, streamlined remnants of plateau material occur within the plains. Each remnant is topped with a 5-km-diameter, partly filled crater. Knobs as much as 1 km across occur throughout the area, but the density is greatest in the southeast. Overlying the smooth plains are craters up to 18 km in diameter.

In the search for a landing site on the west side of the Chryse basin, two areas were photographed. The first, centered on 49°S, 22°N, was photographed on rev 20; the second region, centered at 55°W, 22°N, was photographed on rev 22 (Fig. 1). Both regions, being to the west of the center of the Chryse basin, are at a higher elevation than the area photographed on rev 10.

As anticipated, both these areas show evidence of channeling related to Kasei Vallis and other channels farther south. The rev 20 coverage (which includes the final landing site) can be divided into two halves according to the degree of chan-

neling. In the western half, channel-sculptured terrain is common (Fig. 4); in the east are mainly plains that resemble the lunar maria, and which are a continuation of those described above. They are crossed by ridges which, like those on the lunar mare, usually consist of two parts—a low broad linear rise on top of which is a narrower, more steeply sloping ridge. The ridges are mostly north-south trending and are spaced approximately 40 km apart. The plains surface is less cratered than the lunar maria and several ghost craters suggestive of filling are present. In common with other areas observed, the ejecta around large craters are sharply delineated and appear to consist of several flow lobes. The gradual transition from chaotic ejecta outward into secondary crater fields, characteristic of lunar craters, is rarely seen.

The western half of the area photographed on rev 20 has been extensively modified, apparently by fluvial action. Channels appear to have originated to the west and flowed eastward through the area toward the center of the Chryse basin. The whole region is sculptured by linear channels that wind through the

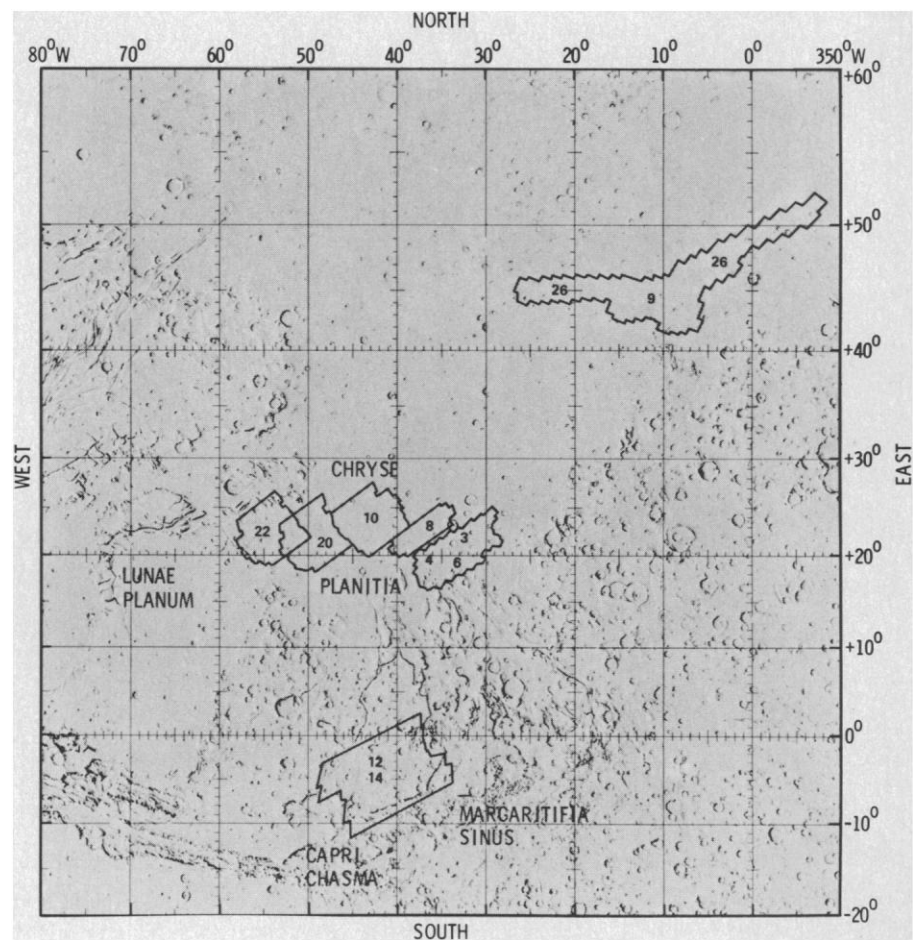


Fig. 1. Index map to show Viking orbital photographic coverage prior to the Viking 1 landing. Orbit numbers for the coverage are indicated. The Viking landing site is in rev 20 coverage.

area and cut across one another. Lenticular bars are common, as are convergent and divergent flow lines. Immediately upstream from the mare ridges sculpturing is often absent as though the fluid pooled there and had little erosive capability. Where gaps occur in the mare ridges the flow lines converge, indicating funneling of the flow through the gap (Fig. 4). Deeply incised channels occur downstream of the gaps. At the southern end of the channeled area the flow appears to have been contained and diverted by a large ridge. The sculptured area over which flow has presumably occurred is approximately 150 km wide. The length of the channels will not be known until more photographs are taken to the southwest. The general impression is of a flood, fairly evenly spread over a large area with very shallow slopes. The northern end of the rev 20 coverage includes part of Kasei Vallis. Again, as in the

south Chryse region, long, lenticular, plateau remnants occur and linear striae attest to east-west flow. A low escarpment with a rectilinear outline, which seems to be unsculptured by flow, marks the edge of Kasei Vallis. The scarp consists mostly of intersecting alcoves that give it a serrated outline, although there are some linear sections. In general, it lacks streamline forms. Isolated areas of plains, surrounded by an escarpment, occur within the Kasei Vallis. Large craters superposed on these escarpments suggest a very old age (Fig. 5).

South of Kasei the region photographed on rev 22 can be divided east-west into two broad areas. In the east is a continuation of the lightly cratered plains. They resemble lunar maria and in the south are extensively sculptured by channel processes. The western half of the region is distinctively different from any region yet photographed. From the

Mariner 9 data, it appears that a narrow strip of ancient cratered terrain separates Lunae Planum from Chryse Planitia. Numerous large craters within the strip typically have subdued rims and indistinct ejecta patterns, somewhat similar to those of the craters in the C site area described below. The plains between craters are, however, extremely hummocky and are crossed by several channels that are distinctly different from those at the C site. A section of one channel, which runs approximately east-west at 21°N, resembles some of the larger lunar rilles, such as Schröters Valley. Other channels farther south have rounded cross sections and numerous tributaries. All appear to empty onto the plains to the east. These channels are quite old with numerous superposed impact craters. The hummocky deposits in the west on the lunarlike mare plains also appear to be relatively old, since ejecta from several large craters covers both upland and plains.

Cydonia region (B1 site). The Cydonia site (revs 9 and 26; 44°N, 12°W), as mapped from Mariner 9 (4), lies near the boundary between the mottled cratered plains and the smooth plains and includes the transitional boundary between mantled and unmantled terrain (5). The area shows a complex history of erosion and deposition. To the west and north, the surface is cut by a complex of curvilinear fractures typically 1 km wide and 10 km long that in plan view forms as a set of roughly polygonal-to-circular forms, most of which are 5 to 20 km across (Fig. 5). Southeast, the fractures seem to be buried by a younger unit that has undergone subsequent erosional stripping. This younger plains unit has a relatively featureless surface apart from superposed degraded craters.

Isolated angular-to-rounded mesas in the south are either (i) the remains of a once-continuous unit which overlay the fractured plains or (ii) the remnants of an ancient eroded surface projecting through the fractured plains from below. The mesas and fractured plains clearly underlie a younger plains unit to the southeast, which indicates that at least one phase of erosion occurred to produce the mesa landforms before deposition and erosion of the plains. Craters on surfaces below the plains are flat floored and have smooth rims surrounded by low, outward-facing scarps.

The youngest unit is a mantle of relatively bright material, probably of aeolian origin, that buried preexisting small craters. Other subsequently formed craters deposited ejecta from lower units on top

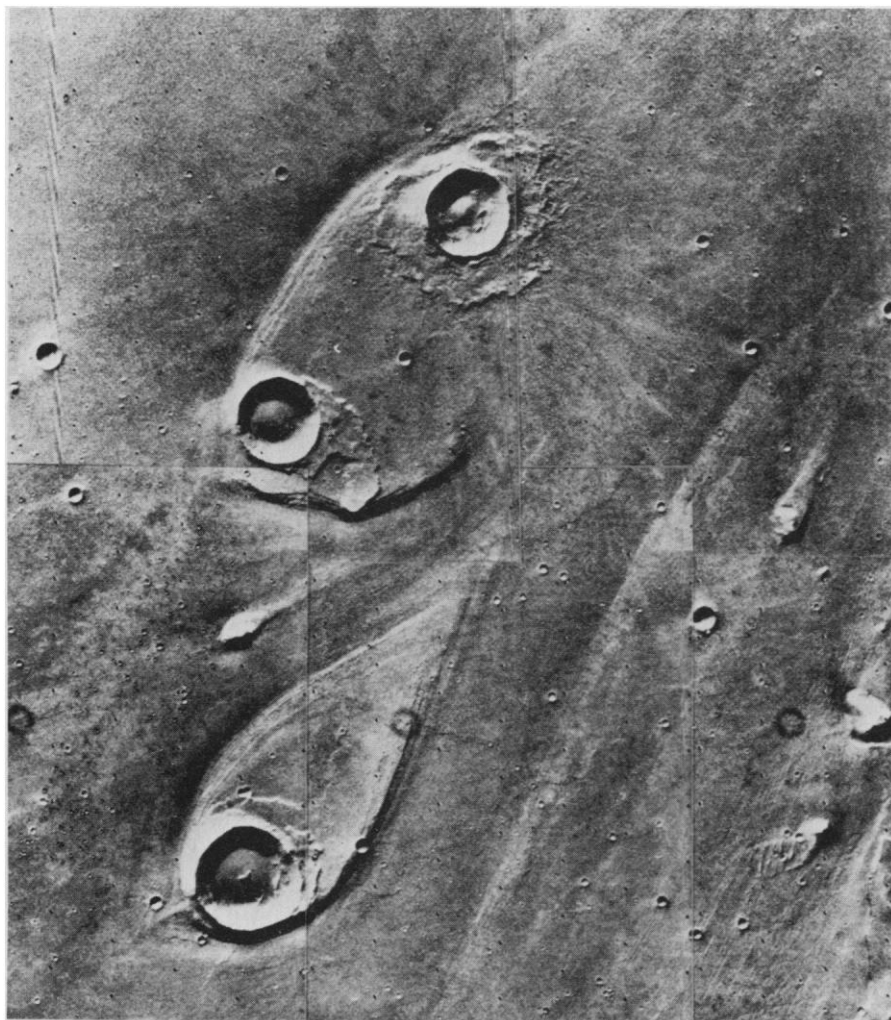


Fig. 2. Photomosaic to show teardrop "islands" on the southern side of the Chryse basin. The islands consist of remnants of the plateau material that forms a more continuous outcrop farther south. Here the plateau material has been largely eroded, apparently by fluvial action; craters on the upstream ends of the islands have protected the plateau material downstream of them from erosion. Each island is about 40 km long (frame numbers 4A50 to 4A54).

of the mantle. During a later phase of erosion most of the mantle in the southern and western part of the area was stripped away, presumably by aeolian activity, leaving material trapped inside small bowl-shaped craters, and under and within ejecta deposits. These remnants of bright materials throughout most of the region give the mottled appearance observed in Mariner 9 and Viking pictures.

The origin of the fractured plains is not immediately apparent. Although the fractures could be the result of cooling contraction of extensive, thick lava, the scale of the pattern is larger by an order of magnitude than is normally found in such rocks. Another possibility is that they are of tectonic origin, but the lack of a marked regional trend to the pattern does not support such an origin. The possibility that they are related to a deep permafrost layer is an attractive alternative. However, this layer of permafrost would have to be abnormally thick. The region shows an extremely complex history of volcanic, tectonic, aeolian, and, possibly, periglacial processes, which yield a complex variety of landforms and materials.

Capri Chasma region (C1 site). On revs 12 and 14, frames were taken of the C site at 6°S, 43°W, one of the alternative sites for the second lander. The site is adjacent to Capri Chasma, a branch of the equatorial canyon system. The area outside the canyon is characterized by numerous large, flat-floored, subdued craters, between which are areas of relatively smooth intercrater plains. North of the site are several areas of chaotic terrain in which several large channels appear to originate. The channels drain northward, converge with other channels, and ultimately debouch into the Chryse basin.

The views of the canyon are some of the most spectacular pictures yet acquired. Landslides (Fig. 6) are clearly visible on both walls. The walls are as much as 2 km high and display several stratigraphic units that erode differentially. The uppermost layer breaks into large blocks while the lower layers seem to have poor cohesion and exhibit more fluid flow. There are a few low hills or knobs on the canyon floor, some of which may be remnants of coherent materials that have slumped into the canyon. Much of the canyon floor is featureless, devoid even of craters at the limiting resolution of the cameras. This suggests that the canyon floor is relatively young, certainly younger than any other surface yet observed on Viking pictures. The presence of bright streaks and dune fields (Fig. 6) indicates an active aeolian regime.

These observations imply that the canyon is enlarged by collapse of the canyon walls to produce debris flows and removal of the material by wind. Although the causes of slope failure are uncertain, groundwater sapping or undercutting by aeolian action (or both) may be contributing processes (6).

Most of the large (> 50-km-diameter) craters in the region are flat-floored and have low rims; their ejecta appears to be covered by intervening plains material, indicating that the craters are older than the plains. However, some large craters are younger than the plains and have well-developed albeit subdued ejecta. Strings of secondary craters are

abundant in some areas. Since Mariner 9, the origin of the intercrater plains has been a subject of some controversy. It has been variously ascribed to ballistic and base surge phenomena associated with impacts (7), atmospherically redistributed impact debris and weathering products (8), and volcanic activity (9). The layers in the canyon wall provide a cross-sectional view of the plains, and the morphology of the landslides provides an impression of the mechanical properties of the near-surface materials. It is possible that coherent layers resistant to erosion form the surface and that they are underlain by more easily erodible, less coherent materials. An inter-



Fig. 3. Photomosaic to show the light-toned, "etched" terrain on the southern side of the Chryse basin. Also shown are light, domical features (v) thought to be volcanic shields. The mosaic covers an area about 60 km from top to bottom (frame numbers 4A78 to 4A81).

pretation of the general terrain of the C1 area is that it is composed of highly brecciated rocks of the ancient cratered terrain overlain by plains-forming deposits. The origin of the plains is not clear but the volcanic hypothesis is supported by the presence on the surface of numerous ridges and scarps similar to those on the lunar maria.

The close relation between fluvial fea-

tures and chaotic terrain, noted on the basis of Mariner 9 observations, is clearly seen in the northern part of the site (Fig. 7). An area of chaotic terrain 50 km across is at the head of a series of fluvial-like features. The surface at the head of the channel appears to have collapsed into a jumbled, chaotic mass of debris, as though the underlying material had been removed. The area to the west

has been sculptured and shaped into streamlined forms, suggesting flow to the west. The channel-like feature can be traced about 400 km to the west, where it passes off the edge of the photographic coverage into the region of the Hydrocates Chaos from which the channels of the Simud Vallis originate. These latter channels lead to Chryse Planitia, where the first Viking has landed. It thus appears that some of the materials that were carried out of the chaotic terrain in the C site ultimately may have been deposited far to the north, close to the present Viking landing site. The origin of the chaos and the channels is still unclear, but massive removal of subsurface materials, including a transporting fluid, is amply demonstrated.

Craters. Craters with fresh ejecta blankets and associated secondary craters were rarely seen in Mariner 9 pictures. It was predicted that, because the surface gravity on Mars is about the same as it is on Mercury, martian craters would have a similar morphology to those on Mercury (10) with the secondary crater fields much closer to the crater rim than on the moon, where the surface gravity is less. Viking pictures, however, show that fresh craters do exist on Mars and that, at least in the areas photographed, their morphology (Figs. 8 and 9) is dissimilar to that on Mercury or on the moon. Fresh craters are surrounded by lobate flow scarps and ridges, outside of which, in some cases, are bright rays and secondary crater clusters. The ejecta were apparently emplaced largely by flow. On arrival at the surface from ballistic throw-out, the ejecta may have transformed to a fluidized sheet, possibly as a result of melted and vaporized ice or entrapped atmospheric gas. The lack of this distinctive ejecta pattern on the moon and Mercury may be explained by their lack of atmospheres and subsurface ice.

Not all martian craters have the same form. Many are degraded to smooth forms with flat floors and are encircled by an erosional scarp that faces outward. However, other apparently fresh craters, such as those near Kasei (Fig. 9), have closely spaced radial lineations on the continuous ejecta and few or no lobate forms. Whether such differences between fresh craters result from different states of target material or from other parameters remains to be determined.

Another striking characteristic of the areas photographed thus far is the presence of fresh crater clusters and irregularly shaped craters similar in form to lunar secondary craters. Some of the smaller clusters can be related to nearby

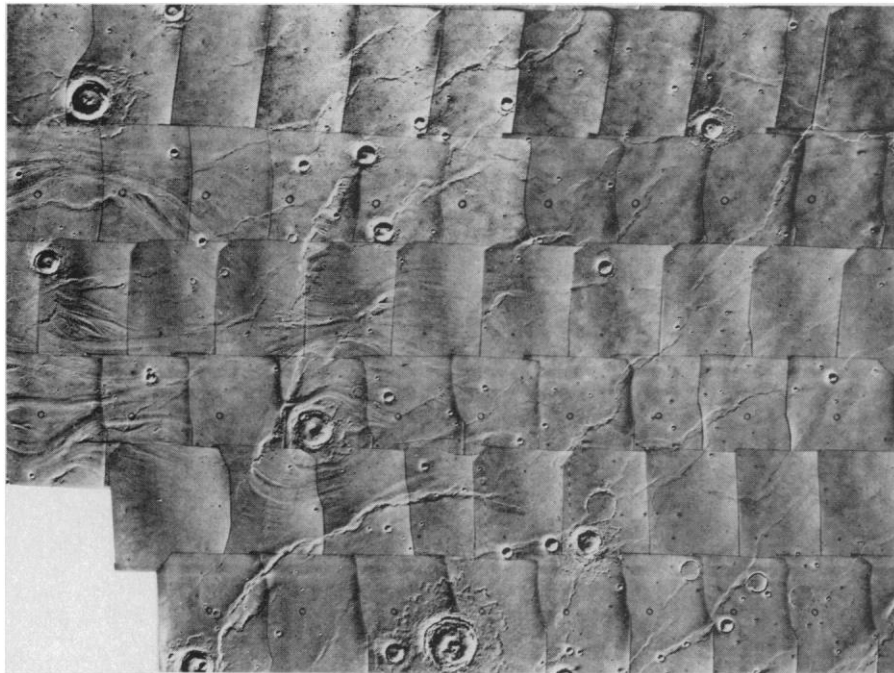


Fig. 4. Photomosaic of the landing site region in Chryse. Channeling is seen to the west (left). To the middle and right the plains have ridges similar in appearance to lunar mare ridges, implying that the plains were formed by extensive lava flows. The distance across the mosaic is about 240 km.

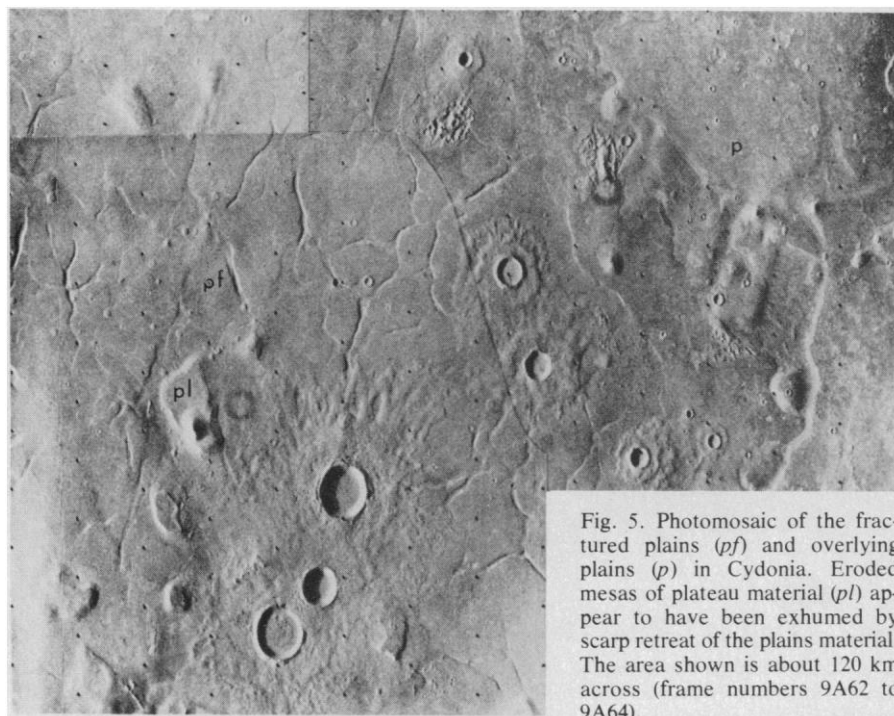


Fig. 5. Photomosaic of the fractured plains (*pf*) and overlying plains (*p*) in Cydonia. Eroded mesas of plateau material (*pl*) appear to have been exhumed by scarp retreat of the plains material. The area shown is about 120 km across (frame numbers 9A62 to 9A64).

fresh craters but there are other, often extensive clusters, particularly at the C site, which are not obviously related to large fresh craters. It is possible that some craters resembling secondary craters result from the impact of meteoroid showers produced by breakup of a large meteoroid on entry into the martian atmosphere.

Variable features. Four types of variable features (11) are prominent in the Viking orbiter pictures: (i) bright streaks associated with craters, (ii) bright streaks associated with small hills, (iii) dark streaks associated with craters, and (iv) sand dune fields. These were compared with the available Mariner 9 coverage to determine the changes that have occurred since 1972. As a result of the increased resolution of the Viking photography, many more small craters and streaks are visible in the Viking images. Comparison with the Mariner 9 data shows that the bright streaks are generally unchanged in direction and outline since 1972, although in a few places they have increased in size or new bright streaks have appeared.

In the Chryse region dark streaks are less prominent than bright streaks and trend southwest to northeast, opposite to the bright streak direction. The dark streak direction coincides with the regional wind flow expected at the present season (northern summer). The bright streak pattern defines wind flow from northeast to southwest, the direction of strong winds that are expected during southern summer dust storms. The directions and outlines of bright crater streaks are unchanged since the Mariner 9 coverage in 1972, thereby confirming the speculations that bright streaks, unlike some dark streaks, are stable over many martian seasons and are unaffected by the weaker winds that occur during the present season. Evidently, the winds responsible for the formation of the dark streaks did not significantly modify the bright ones.

Westward across the Chryse basin the bright streak direction shifts from an azimuth of 220° to 230° near 34°W to 255° near 58°W, a pattern consistent with that observed by Mariner 9. Wind streaks appear to be concentrated in regions that look generally smooth at orbital picture resolution. This correlation of streak density with terrain type may be valid down to roughness scales of tens of centimeters since, for example, in the rev 20 coverage the only large area that appears to be smooth but which is devoid of streaks appear rough to radar. There is supporting evidence, based on

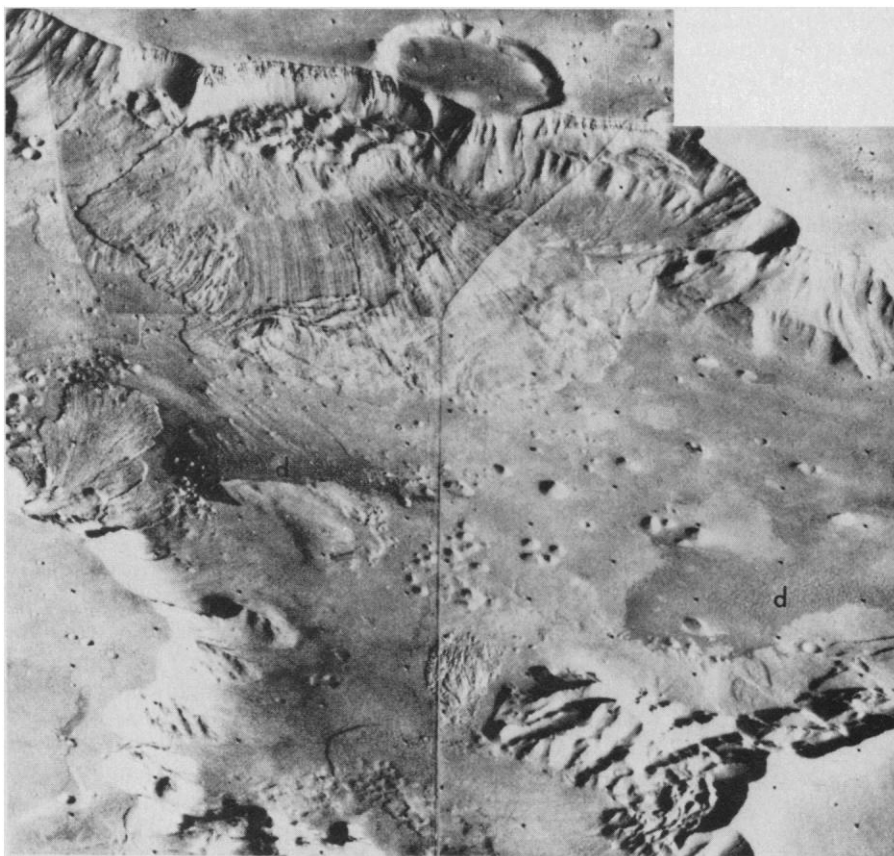


Fig. 6. Oblique view across the Capri Chasma to show dark fields of sand dunes (*d*) in the floor of the canyon, and landslides on the walls. Distance from foreground to background is about 150 km; the canyon is about 2 km deep (frame numbers 14A29 to 14A32).

Mariner 9 data, that wind streaks are best developed in regions where the areas between craters are relatively smooth.

No wind directions in the Cydonia region can be mapped because the area lacks streaks that are associated with craters and other evident wind markers. At least during this season (northern summer), wind transportable material appears not to move; either the texture of the surface is too coarse, or the fine particles are effectively bound together. The annual dust storm fallout that probably blankets the area after perihelic dust storms could be swept up effectively into the numerous troughs which occur in this region. Significantly perhaps, some of the troughs show definite signs of infilling by high albedo material.

In the Capri region, bright streaks trend northeast to southwest and are unchanged in orientation and outline since 1972 (Mariner 9 data). Low albedo dune fields occur on the floor of neighboring Gangis Chasma (Fig. 6). Bright, streaklike markings behind hills on the canyon floor are common in the vicinity of dune deposits and may represent protected areas where no sand has accumulated. The directions of these bright streaks associated with hills show that the domi-

nant regional northeast to southwest wind flow is channeled by the canyon walls into a general east-west direction.

High-altitude pictures of the Oxia Palus region show that the general albedo boundaries and bright streak patterns are unchanged since 1972. Nevertheless, conspicuous albedo changes have occurred in some localized areas, such as within and around the crater Galilaei. A new bright streak, trending south from a 4-km crater, has appeared since 1972, and a streaklike bright area emanating from a channel has grown significantly during the past 4 years. These areas will be studied at high resolution later in the mission.

Atmospheric phenomena. Numerous atmospheric phenomena have been observed in the orbiter camera images, both on approach and from high altitude in orbit. Approach images indicated that the atmosphere of Mars was then relatively clear in the southern hemisphere but obscuring hazes were present at all longitudes in the north. After Mars orbit insertion, most of the high-altitude images were acquired in order to monitor a broad area around the planned landing site for dust activity. In this coverage, taken from a range on the order of 30,000

km, the site is seen in morning hours and each pixel spans about 800 m.

Figure 10 shows a mosaic of a typical high-altitude, five-frame sequence taken through a red filter by the Viking 1 orbiter cameras and processed without spatial frequency discrimination. Although some differences are seen from day to day, the general haziness of the morning sky in the northern hemisphere has looked much like Fig. 10 since Viking 1 arrived. The midday and afternoon skies are not visible for comparison, but the finding of diffuse morning cloudiness is consistent with long-term photography of Mars from Earth. On some days, high-altitude pentads have been obtained through violet and green filters as well as through red, and the overall differences in haziness are not very great.

In regions of Fig. 10 where surface features such as crater rims can be detected, the atmospheric extinction coefficient γ can be estimated from contrast measurements. Where craters are near the threshold of detection, the local values of γ for blue light turn out to be comparable with Earth's atmosphere on a relatively clear day, but values for

red light are somewhat greater than on Earth. When expressed in terms of equal air paths, however, this morning scattering above threshold craters is fully two orders of magnitude greater than in clear Earth air. In regions of similar emission angles where craters exist but cannot be detected, the martian atmosphere is optically still thicker.

The morning haziness in the north that is shown in Fig. 10 would not, on the basis of photography from Earth, be expected to typify other latitudes and times of day. Indeed, Fig. 11a, which was obtained on 11 July 1976, shows a much clearer atmosphere around 50° to 60°S in midafternoon, where the extinction coefficient of red light was found to be $\gamma \sim 0.1$ per air mass. It was approximately winter solstice ($L_s = 93^\circ$) in the southern hemisphere, thus the terminator lies only a few degrees below the bottom of Fig. 11a. In Viking approach images, there were bright patches in this region that did not obscure underlying topography and that contrasted more strongly with their surroundings in violet images than in red, but their nature is not yet clear and further observations are

planned for distinguishing between fog and frost.

Figure 11a, taken at a range of about 18,000 km, also illustrates well the layered structure of the atmosphere. From the foreshortening of craters, we infer the true surface limb to lie about 3 km under the bright low-altitude haze, while upper layers extend to nearly 40 km above the surface. At the limb, the low-altitude haze is optically thick, but the uppermost layer has an edge-on extinction of only about 0.3. This implies that the uppermost layer has a vertical extinction coefficient less than 0.01 per air mass, thus it plays very little role in the total atmospheric obscuration.

The height of the limb haze in the tropics has been estimated in an image from rev 4. Landmarks in the scene were used to locate the surface limb, which was more heavily obscured than in Fig. 11a. In the rev 4 image, the highest visible haze layer occurs at 25 km, and the height of unit optical depth on the limb (normal optical depth ~ 0.02) occurs at 15 km. Since the surface optical depth in the same region as judged from crater contrasts is ~ 0.5 , the scattering power



Fig. 7. Photomosaic of a 120-km-long channeled area near Capri Chasma. The apparent source of the fluid that cut the channels is a depression enclosing chaotic terrain (right) which appears to have been formed by collapse (frame numbers 14A67 to 14A69)

of the atmosphere increases more rapidly with depth less than 15 km than does the atmospheric density. Infrared thermal mapper temperature measurements, which have a very broad weighting function but which center near 20 km, show that the highest tropical haze layers cannot be CO₂ ice.

Discrete clouds, as distinct from diffuse regional haze, seem to have several morphological forms. The classical white clouds of Tharsis, known for decades to observers on Earth, are seen in Fig. 11b, which was obtained through a violet filter at a range of 300,000 km as Viking 1 initially approached Mars. Images taken when this region was clear to the morning terminator do not show these clouds, and we hope that orbital images will provide additional information about their growth phase. They were observed by Mariner 9 only when fully formed (12).

Several diffuse bright clouds of similar size have been seen within the morning

haze in the north. Figure 11c shows one covering about 40 square degrees that appeared near the final A1 landing site on rev 28. It contrasted more with its surroundings in this violet image than in a corresponding red one. Images 6 minutes apart revealed no motion with respect to surface features; an upper limit on its motion is estimated to be 10 m/sec.

Equatorial clouds seen thus far are much less diffuse and are made up of many patches with dimensions of a few kilometers. Figure 12a shows one seen on rev 4 at 23°W, 1°S. It is typical of condensate clouds and showed much higher contrast in violet light than in red. Its motion was 46 ± 3 m/sec westward. Since no shadows were identified, the height of the cloud above the surface is unknown. However, such clouds appear to have a convective structure and are inferred to be within a few kilometers of the surface. Westward cloud motions at speeds ranging from 15 to 45 m/sec

are expected theoretically in this region and at this season (13). This east-west flow is part of an expected anticyclonic circulation around the Chryse basin.

Similar clouds were also detected in low-altitude vertical imaging of candidate landing sites, as illustrated in Fig. 12b, which shows a portion of two C1 site mosaics centered at about 40°W, 4°S. Frames in the second mosaic were taken two martian days after those in the first mosaic under similar viewing conditions. Both sets of frames were acquired through a clear filter and have been processed in such a way as to enhance high spatial frequencies. Sequences designed to provide stereoscopic coverage of the landing sites yield repeated coverage of those regions over time intervals of about 2 minutes. Changes in position and appearance of these cloudlike features over such short time intervals confirms them to be atmospheric phenomena.

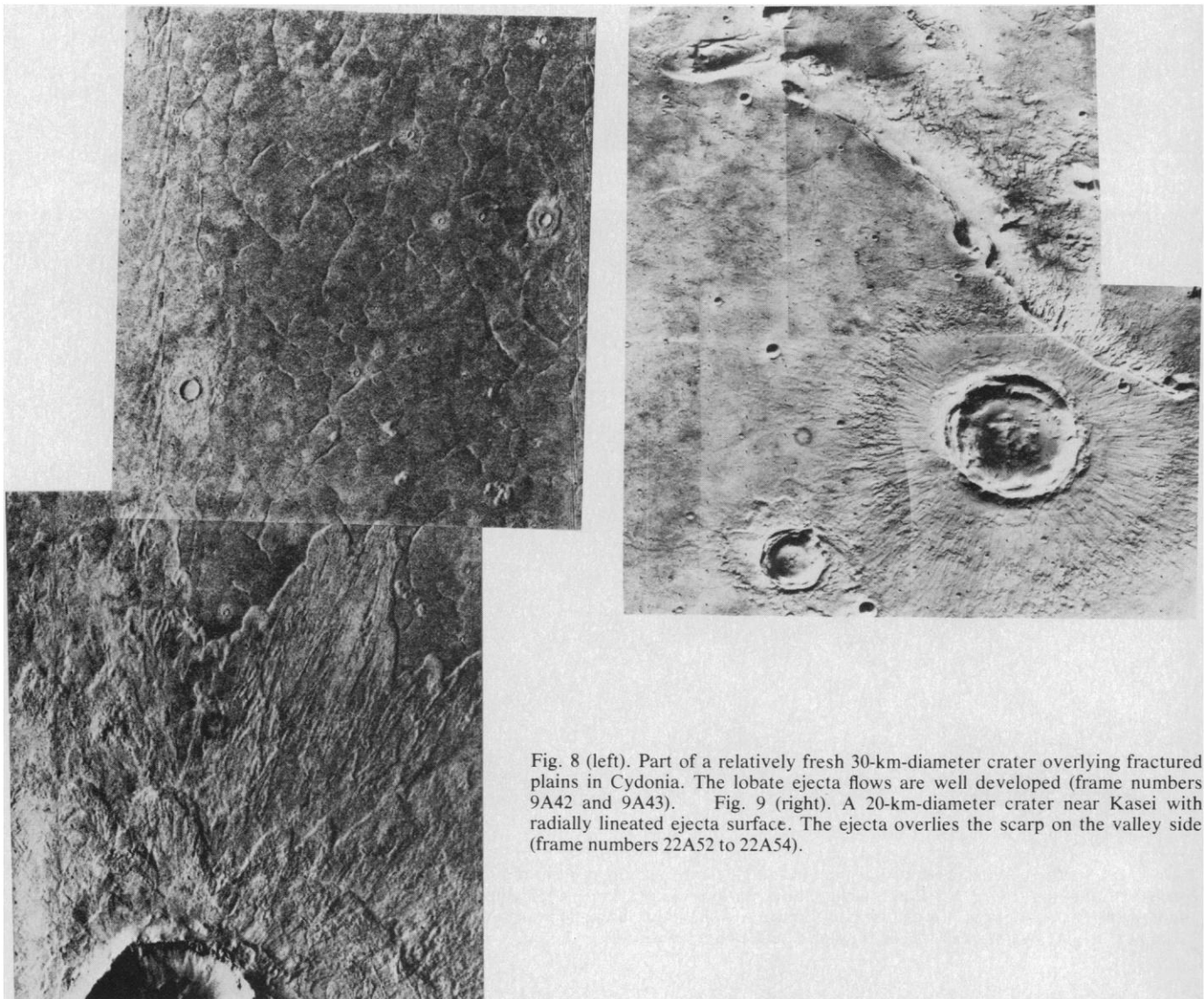


Fig. 8 (left). Part of a relatively fresh 30-km-diameter crater overlying fractured plains in Cydonia. The lobate ejecta flows are well developed (frame numbers 9A42 and 9A43). Fig. 9 (right). A 20-km-diameter crater near Kasei with radially lined ejecta surface. The ejecta overlies the scarp on the valley side (frame numbers 22A52 to 22A54).

Wave clouds have been observed in midmorning images of the equatorial region. A wave pattern can be seen in the

lower left corner of Fig. 12b, but some better examples are found in Fig. 12c. A comparison with frames of the same area

taken on another day indicates that many discrete albedo features in Fig. 12c, such as bright splotches and crater tails, are

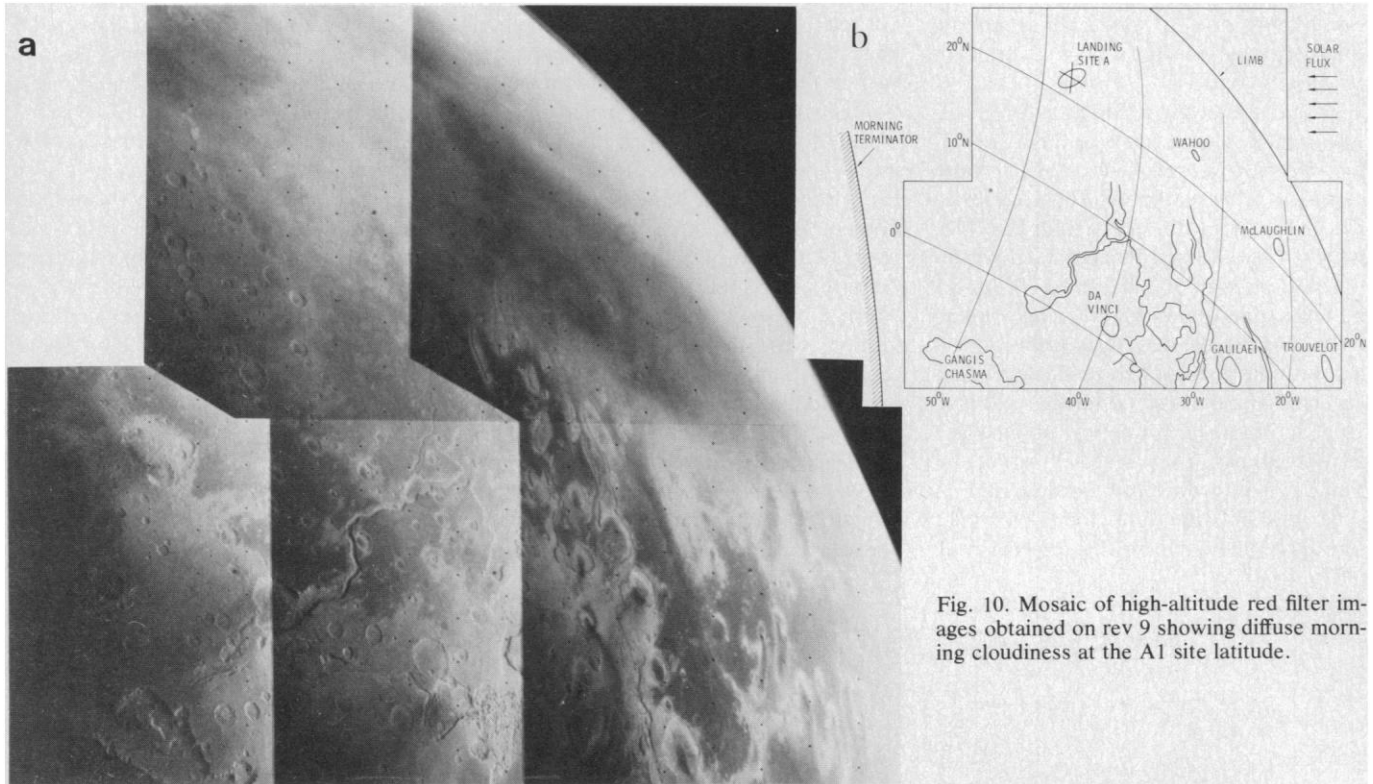


Fig. 10. Mosaic of high-altitude red filter images obtained on rev 9 showing diffuse morning cloudiness at the A1 site latitude.

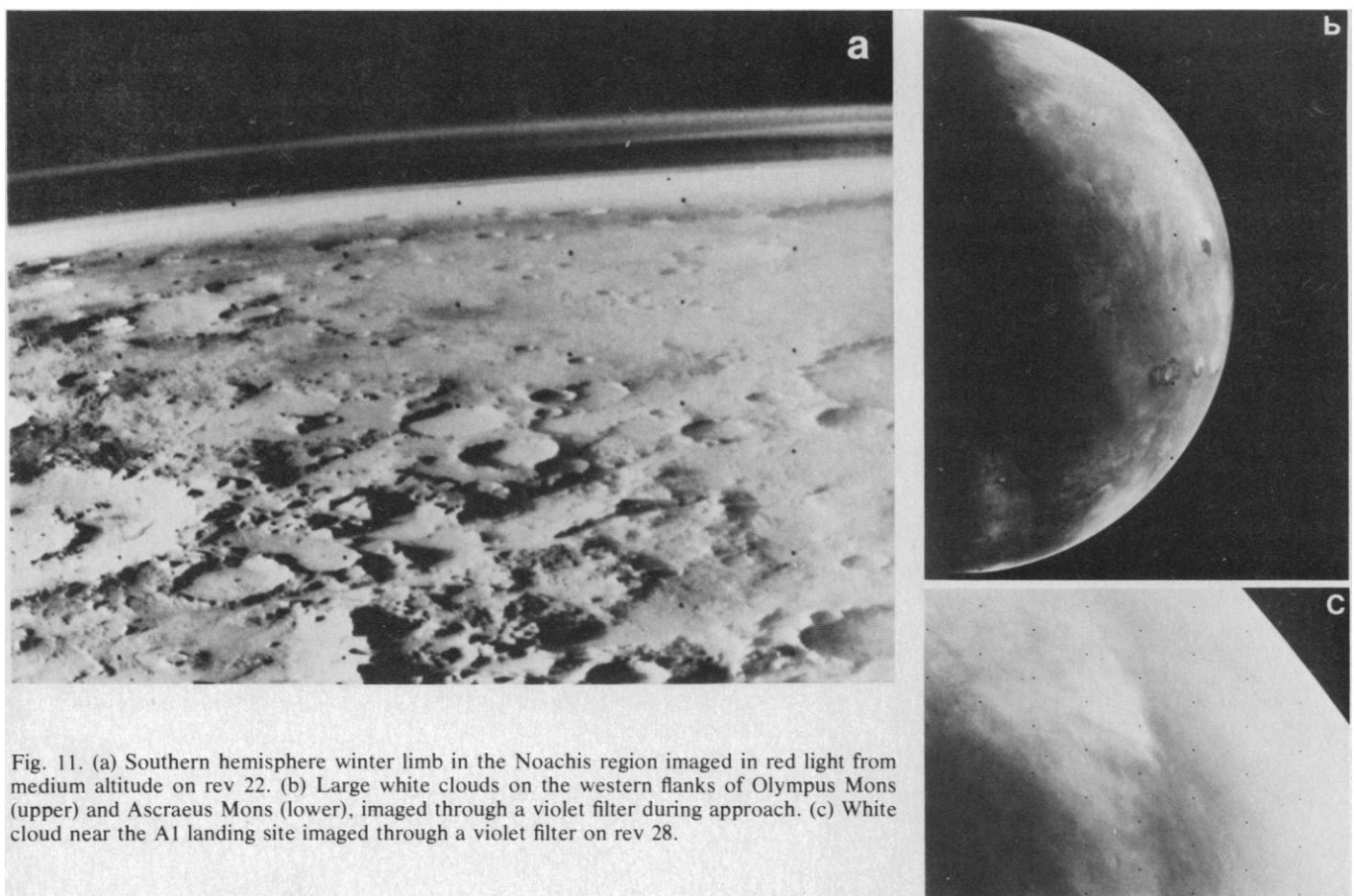


Fig. 11. (a) Southern hemisphere winter limb in the Noachis region imaged in red light from medium altitude on rev 22. (b) Large white clouds on the western flanks of Olympus Mons (upper) and Asraeus Mons (lower), imaged through a violet filter during approach. (c) White cloud near the A1 landing site imaged through a violet filter on rev 28.

on the surface, but that the whole area is overcast with a nonuniform haze. The presence of wave clouds, presumably composed of water ice, provides an indication of the wind direction and of the static stability of the atmosphere (14). Observed wavelengths are on the order of 10 km.

At the lower right of the images in Fig. 12d is a bright patch seen in Capri Chasma from high altitude on rev 4. It does not obscure or diffuse surface detail, therefore it evidently lies closer to the surface than the resolution limit (about 2 km). It may be either a fog of water ice or possibly a thin frost patch. The former seems rather more likely in view of the smaller amount of water required to produce the observed brightness.

No direct evidence for dust clouds has been seen in early Viking 1 orbiter im-

ages, although the presence of micron-size dust particles could well be postulated in some of the haze without contradicting the observed characteristics.

On the basis of preliminary examination of about 1000 frames obtained from Viking 1 orbiter, the following conclusions are reached.

1) Most of the surfaces examined are old. Crater frequencies on the various plains range from one-tenth that of the lunar maria to approximately the same as the lunar maria. Only the floor of Vallis Marineris is significantly younger, on the basis of crater frequencies.

2) Despite the seemingly old age, of almost all the surfaces so far photographed, small craters are preserved, thereby suggesting that aeolian erosion is extremely slow.

3) Abundant new evidence of cata-

strophic floods has been revealed in the southern and western margins of the Chryse basin; however, no evidence for a thick accumulation of sediments was found in the middle of the Chryse basin.

4) One mechanism for growth of the equatorial canyon system is slumping of the canyon walls into the canyon and subsequent removal of the slumped debris by wind.

5) In most of the areas examined, crater ejecta morphology is distinctively different from either the moon or Mercury; the principal mechanism of ejecta emplacement appears to be surface flow rather than ballistic deposition.

6) At 44°N numerous intersecting cracks on the surface of the plains form polygonal patterns reminiscent of patterned ground in the Arctic regions of Earth.

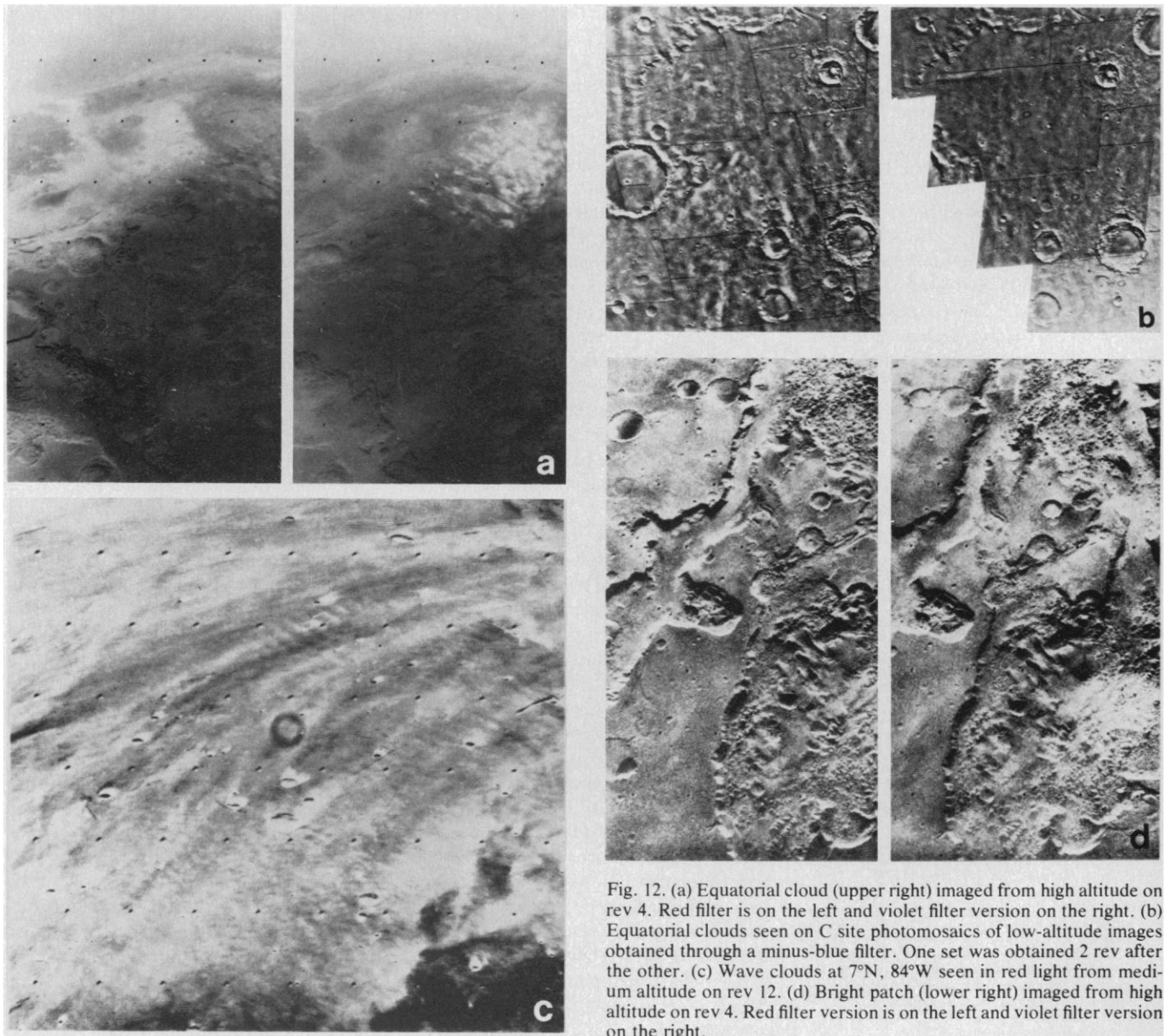


Fig. 12. (a) Equatorial cloud (upper right) imaged from high altitude on rev 4. Red filter is on the left and violet filter version on the right. (b) Equatorial clouds seen on C site photomosaics of low-altitude images obtained through a minus-blue filter. One set was obtained 2 rev after the other. (c) Wave clouds at 7°N, 84°W seen in red light from medium altitude on rev 12. (d) Bright patch (lower right) imaged from high altitude on rev 4. Red filter version is on the left and violet filter version on the right.

7) Variable features, when compared to Mariner 9 pictures taken 4 years ago, show relatively little change.

8) Several types of clouds were observed, including diffuse morning hazes in the northern hemisphere, discrete equatorial white clouds, and extensive wave clouds.

9) A direct measurement of wind velocity from cloud motion was achieved for the first time.

MICHAEL H. CARR

U.S. Geological Survey,
Menlo Park, California 94025

HAROLD MASURSKY

U.S. Geological Survey,
Flagstaff, Arizona 86001

WILLIAM A. BAUM

Lowell Observatory,
Flagstaff, Arizona 86001

KARL R. BLASIUS

Science Applications, Inc.,
Pasadena, California 91101

GEOFFREY A. BRIGGS

Jet Propulsion Laboratory,
Pasadena, California 91103

JAMES A. CUTTS

Science Applications, Inc., Pasadena

THOMAS DUXBURY

Jet Propulsion Laboratory, Pasadena

RONALD GREELEY

University of Santa Clara,
Santa Clara, California 95053

JOHN E. GUEST

University of London Observatory,
London, NW72QS, England

BRADFORD A. SMITH

University of Arizona, Tucson 85721

LAURENCE A. SODERBLUM

U.S. Geological Survey, Flagstaff

JOSEPH VEVERKA

Cornell University,

Ithaca, New York 14853

JOHN B. WELLMAN

Jet Propulsion Laboratory, Pasadena

References and Notes

1. J. B. Wellman, F. P. Landauer, D. D. Norris, T. E. Thorpe, *J. Spacecraft Rockets*, in press; T. E. Thorpe, *Icarus* **27**, 229 (1976).
2. L. Tyler, personal communication.
3. D. H. Wilhelms, *U.S. Geol. Surv.* (1976), p. 1-895; H. Masursky, N. J. Trask, M. E. Strobell, A. L. Dial, G. W. Colton, *U.S. Geol. Surv. Map*, in press; D. Milton, *U. S. Geol. Surv.* (1974), p. 1-894.
4. M. H. Carr, H. Masursky, R. S. Saunders, *J. Geophys. Res.* **78**, 4031 (1973); D. Scott, *U.S. Geol. Surv.*, in press.
5. L. A. Soderblum, T. J. Kreidler, H. Masursky, *J. Geophys. Res.* **78**, 4117 (1973).
6. R. P. Sharp, *ibid.*, p. 4073.
7. M. Malin, thesis, California Institute of Technology (1976).
8. B. C. Murray, L. A. Soderblum, R. P. Sharp, J. A. Cutts, *J. Geophys. Res.* **76**, 313 (1971).
9. D. E. Wilhelms, *ibid.* **79**, 3933 (1974).
10. D. E. Gault, J. E. Guest, J. B. Murray, D. Dzuris, M. Malin, *ibid.* **80**, 2444 (1975).
11. Variable features were first defined during the Mariner 9 mission to mean surface albedo patterns which changed with time; the term has since been used to include all surface forms that are commonly attributed to aeolian or wind processes [C. Sagan *et al.*, *J. Geophys. Res.* **78**, 4163 (1973)].
12. C. B. Leovy *et al.*, *ibid.*, p. 4252.

13. J. B. Pollack, C. B. Leovy, Y. Mintz, W. Van Camp, *Geophys. Res. Lett.*, in press; P. W. Webster, in preparation.
14. J. A. Pirraglia, *Icarus* **27**, 517 (1976).
15. We thank the following people for their untiring help during the early hectic stages of this mission: J. Boyce, P. S. Butterworth, K. W. Farrell, E. A. Flinn, H. Ferguson, A. Jankevics, K. P. Kaasen, C. Leavy, B. Lucchitta, J. Mac-

Queen, T. E. Poe, Jr., G. Schaber, A. Spruck, E. E. Theiling, D. T. Thompson, and T. E. Thorpe. Financial support for the work of team members was provided by NASA Viking Project Office, NASA Office of Planetary Geology (R.G.), and U.K. Natural Environment Research Council (J.E.G.).

26 July 1976

Viking: Mars Atmospheric Water Vapor Mapping Experiment— Preliminary Report of Results

Abstract. *Observations made from the Viking 1 orbiter show very little water vapor in the Mars atmosphere in the southern hemisphere (0 to 3 precipitable micrometers) with a gradual increase across the equator to northern latitudes. Maximum amounts between 20 and 30 micrometers have been observed in the short period covered by the observations to date. The season, northern midsummer, corresponds to the beginning of the water vapor cycle in that hemisphere. A strong repetitive diurnal cycling between the solid and vapor phases is observed at a site to the east of the Tharsis Ridge at 10° north latitude; the vapor lies close to the martian surface and is most probably in saturation equilibrium with a surface haze or fog throughout much of the day.*

The water vapor mapping experiment is designed to determine the variability of the martian atmospheric vapor over a wide range of spatial and temporal scales. In order to separate the effects of spatial (global and vertical) and time-dependent (diurnal, seasonal, and perhaps longer-term) characteristics, the study must take advantage of the maximum flexibility available from the orbital coverage of the planet, particularly in securing nonsynchronous observation periods (1) and continuing through the seasonal progression obtainable from the Viking extended mission. Many of the characteristics of the martian water vapor, and especially those related to its variability, have been indicated by the behavior observed from Earth-based measurements (2, 3), and the strategy for the present Viking orbital study is based in large part on a model for the interaction between the planet's atmosphere and surface or subsurface material which the past observations have suggested. Thus, one of the principal objectives of the Viking measurements is to refine or revise this model; in this context, the present report must be of a very preliminary nature, since only a very restricted set of measurements made over a relatively short time span from synchronous orbit has been possible so far. The period covered is from approach [Mars orbit insertion (MOI) - 2 days] through Viking 1 lander separation (rev 30), during which emphasis has of necessity been placed on observations related to the characterization of the landing sites. Therefore, many of the water vapor mapping observation sequences necessary for the investigation as a whole have not yet been initiated.

It is pertinent at the outset to comment on the timing of the measurements reported here with respect to the seasonal variation of martian water vapor. Orbit insertion occurred (19 June 1976) when the planetocentric longitude (L_s) of Mars was 84° ($L_s = 90°$ corresponds to the northern summer solstice). The accumulation of data from Earth-based observations has revealed a seasonal variation, the appearance of the vapor coinciding approximately with midsummer in each respective hemisphere and the maximum being reached some 2 months later. (The period of high vapor content and the time interval between the solstice and the maximum atmospheric vapor abundance are longer in the south than in the north.) Maximum values of about 50 precipitable micrometers (pr μm) averaged over a horizontal scale of $\sim 10^3$ km have been observed for both hemispheres, with the maximum apparently occurring at temperate latitudes. Against this framework, the present observations have been made at the onset of the northern "wet" season, and have so far covered the southern (dry) hemisphere and northern latitudes to about 20°, with a few isolated afternoon measurements in the latitude band 40° to 50°.

Instrument and observations. The instrument, the Mars atmospheric water detector (MAWD), is a grating spectrometer operating in the 7200 cm^{-1} (1.4 μm) water vapor bands. Absorption by the atmospheric vapor of solar radiation diffusely reflected from the surface of the planet is measured by five radiatively cooled PbS detectors located in the exit focal plane of the instrument. The detectors are arranged so that, when the grat-